Gram-scale synthesis and unraveling the activity origin of atomically dispersed Co-N₄O sites toward superior electrocatalytic oxygen reduction

Sike Zhang [a,1], Qixing Zhou [a,b,1], Linya Fang [a], Rui Wang [a], Tingyu Lu [a], Qun Zhao [c], Xuefang Gu [c], Shu Tian [c], Lin Xu [a], Huan Pang [d], Jun Yang [e], Yawen Tang [a], Shuhui Sun [f,*]

[a] School of Chemistry and Materials Science, Jiangsu Key Laboratory of New Power Batteries, Jiangsu Collaborative Innovation Centre of Biomedical Functional Materials, Nanjing Normal University, Nanjing 210023, PR China
[b] School of Chemistry and Chemical Engineering, Southeast University, Nanjing 211189, PR China
[c] College of Chemistry and Chemical Engineering, Nantong University, Nantong 226019, PR China
[d] School of Chemistry and Chemical Engineering, Yangzhou University, Yangzhou 225009, PR China
[e] State Key Laboratory of Multiphase Complex Systems, Institute of Process Engineering, Chinese Academy of Sciences, Beijing, 100190, P. R. China, Nanjing IPE Institute of Green Manufacturing Industry, Nanjing 211100, Jiangsu, China
[f] Institut National de la Recherche Scientifique (INRS), Centre Énergie Matériaux Télécommunications, Varennes, Québec J3X 1P7, Canada

ARTICLE INFO

ABSTRACT

Exploring highly efficient nonprecious metal-based single-atom catalysts (SACs) toward the electrocatalytic oxygen reduction reaction (ORR) is critical for the sustainable development of ORR-related energy conversion and storage systems. However, the scalable synthesis, delicate regulation of the coordination environment and molecular-level elucidation of the electrocatalytic mechanism remain challenging. Herein, we report a facile gram-scale synthesis of atomically dispersed Co sites anchored on N-doped carbon nanofibers (noted as Co-SA@N-CNFs) via a reliable predesigned phenolic resin-mediated strategy for efficient oxygen reduction electrocatalysis. The local coordination configuration of the single-atomic Co sites is proposed as the Co-N₄O moiety with one O atom in the axial direction perpendicular to the Co-N₄ plane. Theoretical calculations uncover that, compared with the common Co-N₄ single sites, the formation of Co-N₄O configuration is beneficial to reduce the reaction energy barrier, adjust the bond length between the metal sites and the intermediates, and also increase the electric conductivity. Therefore, the Co-SA@N-CNFs demonstrated distinguished ORR activity, outstanding electrochemical stability and methanol tolerance in KOH electrolyte. Furthermore, when assembled in liquid and flexible solid-state rechargeable zinc-air batteries (ZABs), the Co-SA@N-CNFs-equipped ZABs exhibited higher power densities, larger specific capacities and extraordinary cycling performance, compared with the Pt/C-based ZABs. The simple and robust methodology for the mass production of SACs and the engineered coordination environment for performance optimization inspire the future design of a wide range of SACs for energy devices.

1. Introduction

In response to the rapid depletion of fossil fuels and related environmental pollutions, tremendous endeavors have been devoted to the exploration of a variety of eco-friendly and sustainable energy conversion/storage technologies. [1] Particularly, the oxygen reaction-based renewable energy devices, for instance, metal-air batteries [2–4] and fuel cells [5–8], have recently attracted great research interests because of their favorable energy density and ecological benignity. [9] The output power density and overall energy efficiency of these devices are directly determined by the cathodic oxygen reduction reaction (ORR), [10–13] which involves complicated electron transfer pathways and suffers from sluggish kinetics. [14] To date, platinum (Pt)-based materials are the commonly used ORR electrocatalysts, whereas their low abundance, high price, and vulnerable CO/methanol poisoning have drastically restricted their widespread commercialization. [15] To this end, developing highly efficient non-precious ORR electrocatalysts as promising alternatives to Pt is of practical significance and urgency, but remains a grand challenge.

Over the past decade, transition metal (TM = Fe, Co)-based single-

atom catalysts (SACs), [16–22] which are made of atomically isolated active sites coordinated with support (e.g., N-doped carbon),[23–25] have stimulated extensive attention in the catalysis community thanks to their unique advantages, including maximized atom utilization efficiency, tunable electronic features, and exceptional catalytic activities. [26–28] In particular, Co-N-C catalysts with suppressed Fenton reaction compared with the widely investigated Fe-N-C catalysts have emerged as a class of promising efficient ORR electrocatalysts.[29–31] For the SACs, due to the strong coordination effect between the central metal atom with the neighboring ligands (such as C, N, and O) in the support, [32–35] the electronic microenvironment of the metal center could be finely regulated by altering the coordination numbers, introducing multiple heteroatoms, adjusting the binding configuration, which in turn allows optimizing their intrinsic activity and stability. [29,36,37] Despite the unique advantages of SACs, it still remains a great challenge for the controlled synthesis of SACs. [38] To date, a variety of synthetic methods have been developed, such as mass-selected soft-landing method, atomic layer deposition (ALD) technique, impregnation and co-precipitation, coordination site construction, defect design, *etc*. [27, 39,40] Nevertheless, most of these reported protocols usually suffer from tedious and complicated procedures, unpredictable control of the homogeneity of active sites, low yield, and high production cost, eventually hampering the development and practical industrial applications of SACs. [41] In this regard, developing a reliable and straightforward synthetic methodology for the mass production of SACs with excellent repeatability is particularly attractive and highly desired, yet still remains technically challenging.

Herein, we demonstrate a gram-scale fabrication of atomically isolated Co sites immobilized on N-doped carbon nanofibers (named as Co-SA@N-CNFs hereafter) via a facile "phenolic resin nanofiber-mediated" synthetic strategy. The abundant surface functional groups on phenolic resin nanofibers allow to effectively capture and spatially isolate the Co precursors, preventing the metal precursors from clustering during the subsequent processing. The local coordination configuration of the single-atomic Co sites is proposed as the Co-N$_4$O moiety with one O atom in the axial direction perpendicular to the Co-N$_4$ plane. The high density of atomically dispersed Co active sites and fibrous conductive networks endow the Co-SA@N-CNFs with outstanding electrocatalytic ORR activity, superior robustness and excellent methanol tolerance in KOH electrolyte, exceeding the benchmark Pt/C catalyst. Furthermore, density functional theory (DFT) calculations elucidate that the formation of Co-N$_4$O configuration can induce the optimization of the reaction pathways, alteration of the bond length between the Co sites and the *OOH species, and improvement of the electron transfer capability, therefore significantly lowering the reaction energy barrier and accelerating the electrocatalytic ORR process. More importantly, when assembled the Co-SA@N-CNFs in liquid and flexible solid-state rechargeable Zn-air batteries (ZABs) [42], the devices demonstrated high power densities, large specific capacities, and extraordinary long-term cycling performance, overmatching the commercial Pt/C-based counterparts and suggesting the promising application potential of Co-SA@N-CNFs in renewable energy storage and conversion devices.

2. Experimental section

2.1. Synthesis of Co-SA@N-CNFs

0.5 g of C$_6$H$_7$NO, 1 g of HMTA and 0.05 g of CTAB were dissolved into 50 mL of deionized water and then transferred into an autoclave reactor (Anhui Kemi Machinery Technology Co., Ltd) at 85 °C for 12 h to fabricate the PR NFs aerogel. Subsequently, the as-made PR NFs and 0.3 mmol of Co(NO$_3$)$_2$·6 H$_2$O were dispersed in 30 mL of deionized water and stirred at 25 °C for 24 h to allow the PR NF to adsorb the cobalt ions. Finally, the sample was carbonized in N$_2$ at 900 °C for 1 h. For the mass production, the quantity of feeding chemicals could be scaled up to 50

times.

3. Results and discussions

3.1. Synthesis and structural characterization of Co-SA@N-CNFs

Fig. 1 schematically illustrates the overall preparation procedure of Co-SA@N-CNFs which mainly involves three major procedures: (1) fabrication of phenolic resin nanofibers (PR NFs) via a simple self-catalyzed aldol condensation reaction, (2) electrostatic adsorption of cobalt ions (Co^{2+}) onto the resultant PR NFs, (3) pyrolysis of the formed Co^{2+}-containing PR NFs into atomically isolated Co sites anchored on the nitrogen-doped carbon nanofibers (N-CNFs). Specifically, uniform PR NFs (Fig. S1) were firstly synthesized through the polymerization between 3-aminophenol and hexamethylenetetramine (HMTA) with the assistance of the structure-directing agent of cetyltrimethylammonium bromide (CTAB). [43] During the sol-gel synthesis at 85 °C, HMTA, a frequently adopted curing agent in phenolic resin fabrication, hydrolyzed into ammonia and formaldehyde gradually. Driven by the catalytic role of the generated ammonia and amino groups in the precursor, the in-situ released formaldehyde polymerized with 3-aminophenol to produce phenolic resin. Meanwhile, with the assistance of the rod-like micelles of CTAB molecules at the critical micelle concentration (CMC), the formed PR spontaneously self-assembled into PR NFs through the Coulombic attraction forces with the CTAB rod-like micelles. Interestingly, the rich amino (-NH$_2$) and hydroxyl (-OH) groups on the surface of the PR NFs enable the effective trap of Co^{2+} by the robust electrostatic interaction, allowing the uniform dispersion of the metal precursor on the substrate at the molecular scale. During the final carbonization treatment, the PR NFs were transformed into N-CNFs and the cobalt ions were transformed into atomically dispersed Co sites confined onto the N-CNFs, yielding the targeted Co-SA@N-CNFs. Due to the cost-effectiveness of the raw materials, mild reaction conditions, operation convenience, and time-saving procedures, the designed synthetic protocol herein is highly promising to realize mass production by simply scaling up the feeding amounts of precursors and employing larger reactors.

The representative scanning electron microscopy (SEM) images (Fig. 2a-c) indicate that the Co-SA@N-CNFs can perfectly retain the initial one-dimensional fibrous morphology without structural damage after the pyrolysis treatment, indicating the excellent mechanical robustness. These randomly aligned nanofibers with lengths up to several micrometers interconnect with each other to form the continuous reticular network, which is propitious to mass transport and charge transfer during the electrocatalysis course. The typical transmission electron microscopy (TEM) image (Fig. 2d) again verifies the cross-linked nanofiber structure of the Co-SA@N-CNFs with an average nanofiber diameter of ~ 20 nm. It is worth mentioning that neither obvious nanoparticles nor clusters can be found from the magnified TEM image (Fig. 2e), indicating that Co species might exist as the atomically dispersed form. To further confirm it, an aberration-corrected high-angle annular dark-field scanning transmission electron microscope (AC HAADF-STEM) with atomic resolution is carried out. A great deal of isolated bright dots indicated by the circles are attributed to the heavier Co atoms (Fig. 2f). The HAADF-STEM image and elemental mappings (Fig. 2g) reveal that Co, C, N, and O elements are uniformly distributed throughout the carbon nanofibers. The inductively coupled plasma optical emission spectroscopy (ICP-OES) analysis indicates that the weight ratio of Co in Co-SA@N-CNFs is 1.8 wt%. Notably, the as-developed "phenolic resin nanofiber-mediated" strategy exhibits the capability for large-scale catalyst production. Over 10.0 g of Co-SA@N-CNFs can be conveniently produced in one batch with a high yield (Fig. 2h-j), demonstrating great potential for practical application. Neither metallic Co diffraction peaks nor Co nanoparticles can be detected in the XRD pattern (Fig. S2a) and HRTEM image (Fig. S2b) of the large batch sample, respectively. The AC HAADF-STEM (Fig. 2k) affirms the atomic
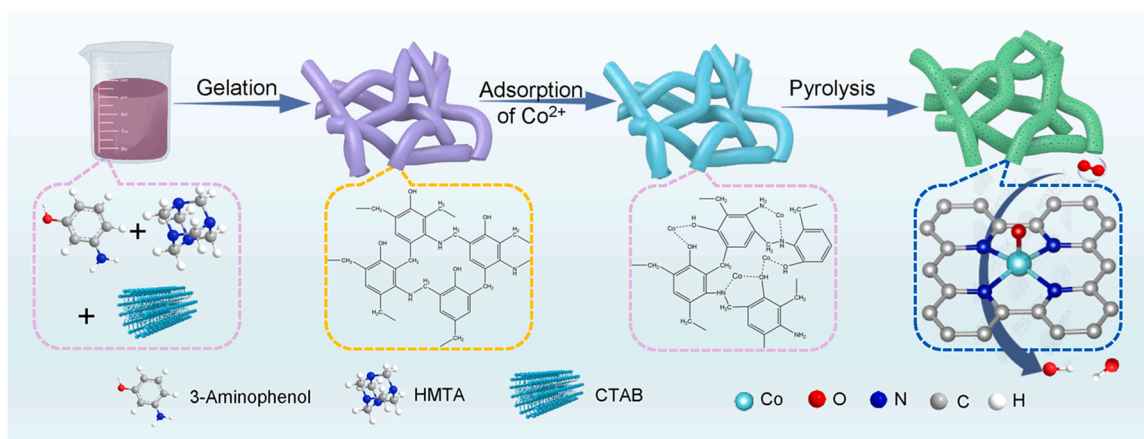
Fig. 1. Schematic illustration of the essential fabrication strategy of Co-SA@N-CNFs.

dispersion of Co in the formed large batch sample, further testifying the excellent scalability and reproducibility of the developed synthetic protocol.

The X-ray diffraction (XRD) pattern (Fig. 3a) of the as-prepared Co-SA@N-CNFs displays only two broad diffraction peaks positioned at 2θ of ~25 and ~43 °, corresponding to the (002) and (100) planes of graphitic carbon, respectively. Moreover, the absence of the diffraction peaks of Co-based species further confirms the single-atomic feature of the Co in Co-SA@N-CNFs. For the Raman spectrum (Fig. 3b) of Co-SA@N-CNFs, the two predominated peaks at 1350 and 1602 cm^{-1} can be ascribed to the disorder sp^3-hybridized carbon (D band) and graphitic sp^2-hybridized carbon (G band), respectively. Moreover, the D band to G band intensity ratio (I_D/I_G) is 0.95, indicating a high graphitization degree of the carbon substrate which ensures excellent electric conductivity of the as-prepared Co-SA@N-CNFs. The low-temperature N$_2$ sorption isotherms (Fig. S3) of Co-SA@N-CNFs can be categorized as the typical type IV isotherm, which exhibits a well-defined hysteresis loop in the relative pressure (p/p_0) range of 0.8–1.0 and thus suggests the existence of mesopores in the Co-SA@N-CNFs. The Brunauer–Emmett–-Teller (BET) specific surface area of Co-SA@N-CNFs is measured as high as 871.78 m^2 g^{-1}, which is beneficial to improve the accessibility of the active sites and promote the mass transport, thus improving the electrochemical reaction kinetics. X-ray photoelectron spectroscopy (XPS) is performed to investigate the chemical composition and valence state of the Co-SA@N-CNFs. The survey spectrum (Fig. S4a) suggests the detection of Co, N, C, and O elements from the surface of Co-SA@N-CNFs. The Co 2p spectrum (Fig. S4b) can be deconvoluted into Co 2p$_{3/2}$ and Co 2p$_{1/2}$ peaks, as well as their shake-up satellite peaks.[44] The prominent deconvoluted peaks at 777.5 and 780.6 eV can be assigned to Co and Co^{2+} species, respectively. The N 1 s spectrum (Fig. S4c) can be well fitted in to five peaks located at 398.1, 398.9, 400.3, 401.0, and 402.3 eV, which are corresponding to pyridinic-N, N coordinated with Co sites (Co-N), pyrrolic N, graphitic N, and oxidized N, respectively. Noticeably, the predominance of pyridinic N and graphite N is believed to be beneficial to generate active sites and meanwhile improve the electrical conductivity. The C 1 s spectrum (Fig. S4d) suggests the presence of C-C (284.6 eV), C-N (285.6 eV), C═O (287.6 eV), and C-O (291.0 eV) bonds.

To precisely probe the fine structure and coordination environment of the single atomic Co sites in the Co-SA@N-CNFs, the extended X-ray absorption fine structure spectroscopy (EXAFS) was further carried out. Furthermore, reference samples of Co foil, CoO, and Co phthalocyanine (Co Pc) were also investigated for comparison. The Co K-edge X-ray absorption near-edge structure (XANES) spectra (Fig. 3c) shows that the absorption near edge of Co-SA@N-CNFs is positioned between those of Co foil and CoO, suggesting that the valence state of the Co moiety in Co-SA@N-CNFs is situated between 0 and + 2. The Fourier transform (FT)

k^3-weighted EXAFS curves (Fig. 3d) indicate that the Co-SA@N-CNFs exhibit only a prominent peak at 1.41Å, attributing to the Co-N (or Co-O) first coordination shell. In addition, no obvious characteristic peak corresponding to Co−Co coordination (2.17 Å) is observed in Co-SA@N-CNFs, which indicates that no Co-based clusters or nanoparticles are generated and the Co sites exist in the atomically isolated form, being in well agreement with the above AC HAADF-STEM findings. To further validate this hypothesis, the least-squares EXAFS fitting is further conducted to acquire the structural parameters and gain the quantitative coordination configuration of the Co sites in Co-SA@N-CNFs. Fig. 3e and Table S1 display the EXAFS best-fitting curves and structural parameters, respectively. The coordination numbers of Co-N and Co-O are fitted to be 3.7 ± 0.6 and 1.5 ± 0.6 with the simulated Co-N and Co-O bond lengths of 1.95 ± 0.05 and 2.12 ± 0.06 Å, respectively. These findings demonstrate that the single Co center in Co-SA@N-CNFs might coordinate with four N atoms and one O atom in the axial direction perpendicular to the Co-N$_4$ plane, forming a Co-N$_4$O configuration (Fig. 3f). Due to the higher binding energies of N and O as compared with C, it is supposed that the coordination of Co with N and O may not only facilitate to modulate the chemisorption behavior of the reaction intermediates for electrocatalysis, but also help to tightly immobilize the isolated single Co sites through the formation of chemical bonds induced by the electron redistribution on the defective sites. The wavelet transforms (WT) of Co K-edge EXAFS oscillations (Fig. 3g) affirm that Co-SA@N-CNFs exhibit a WT intensity maximum at 4 Å^{-1}, which arises from the Co−N/O bond and is distinctly different from the Co-Co coordination. Therefore, it is reasonably inferable that the Co atoms in Co-SA@N-CNFs exist as the mononuclear Co centers with a coordination configuration of Co-N$_4$O based on AC HAADF-STEM observation and EXAFS results.

3.2. Electrocatalytic ORR performance of Co-SA@N-CNFs

It is well accepted that the pyrolysis temperature exerts a key effect in determining the structural feature, graphitization degree and ultimately the electrocatalytic performance of the derived carbon materials. Therefore, a set of temperature-dependent experiments were carried out to obtain the optimal pyrolysis temperature. For the standard synthesis of Co-SA@N-CNFs, the pyrolysis temperature is set as 900 °C. As displayed in Fig. S5, it is found that the final products derived at 800 and 850 °C exhibit similar morphological features and chemical components with the standard Co-SA@N-CNFs. Whereas, the Raman spectra (Fig. S6) reveal that the graphitization degrees of the obtained products are lower than that of the standard Co-SA@N-CNFs. On the contrary, the elevation of pyrolysis temperature to 950 °C resulted in the formation of CoO phase embedded in the N-CNFs, instead of atomically dispersed single Co sites. Therefore, the optimal pyrolysis temperature is deliberately set
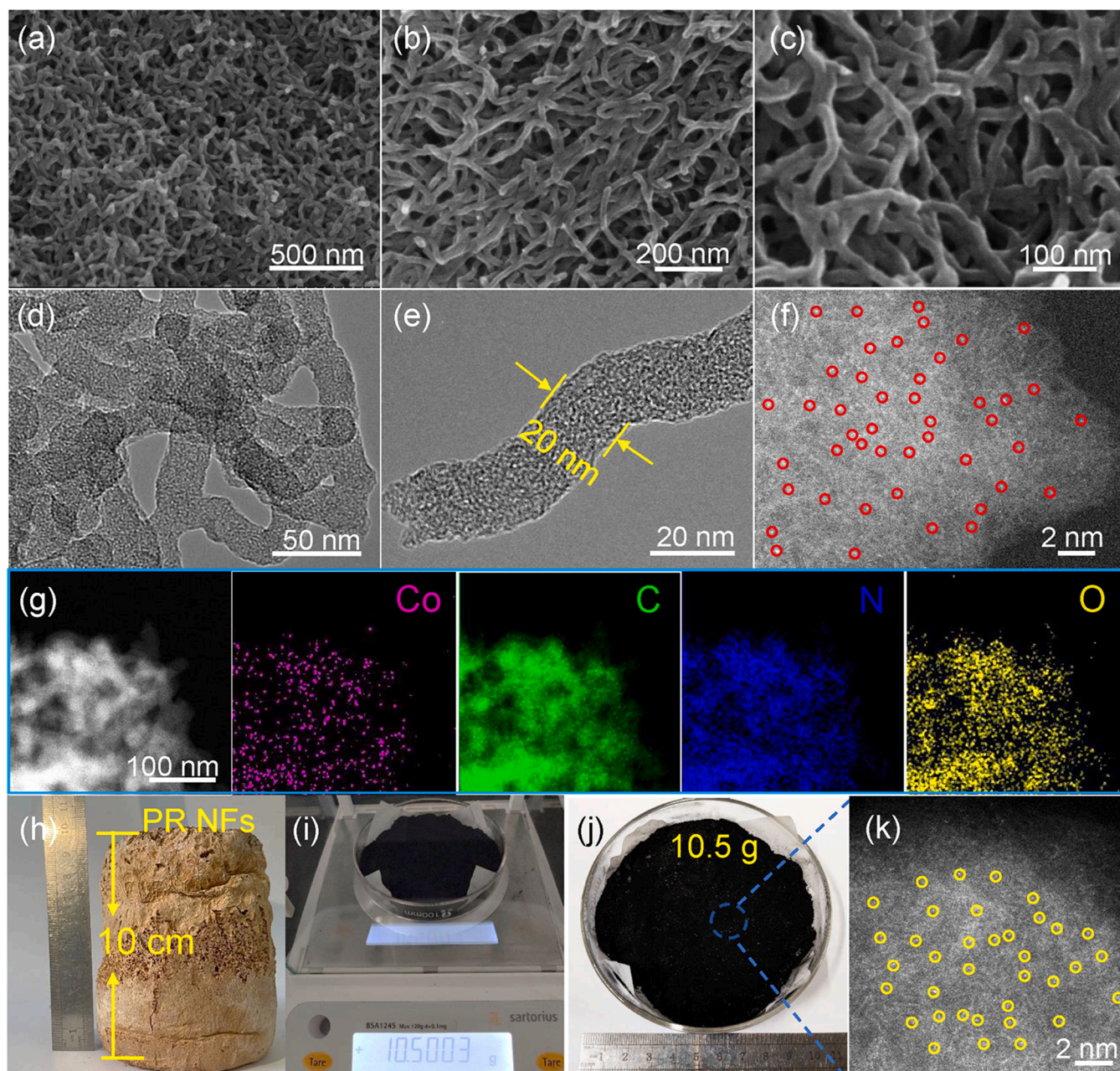
Fig. 2. Morphological characterizations of the as-prepared Co-SA@N-CNFs. (a)-(c) SEM images, (d)-(e) TEM images, (f) AC-HAADF-STEM image, (g) HAADF-STEM image and elemental mapping images (h) picture of mass production of PR NFs, (i)-(j) picture of ~ 10.5 g of Co-SA@N-CNFs, and (k) AC-HAADF-STEM image.

at 900 °C to harvest well-dispersed Co single sites with favorable graphitization degree. For simplicity, the products obtained at 800, 850, and 950 °C are named as Co-SA@N-CNFs-800, Co-SA@N-CNFs-850, and CoO@N-CNFs hereafter, respectively.

The electrocatalytic performance of Co-SA@N-CNFs toward ORR was examined in O_2-saturated 0.1 M KOH solution using a standard three-electrode configuration. In addition, Co-SA@N-CNFs-800, Co-SA@N-CNFs-850, CoO@N-CNFs, N-doped carbon nanofibers without Co pyrolyzed at 900 °C (N-CNFs, Fig. S7) and commercial Pt/C (20 wt%) catalysts were also tested under the identical test condition for comparison. The linear sweep voltammetry (LSV) curves (Fig. 4a) suggest that N-CNFs and CoO@N-CNFs exhibit very poor ORR activities with the considerably negative half-wave potentials ($E_{1/2}$) and small limited diffusion current densities, while the standard Co-SA@N-CNFs synthesized at 900 °C shows the best ORR activity with the most positive $E_{1/2}$. As shown in Fig. S8, the $E_{1/2}$ of the standard Co-SA@N-CNFs is 0.85 V,

which is superior to that of Co-SA@N-CNFs-800 (0.77 V), Co-SA@N-CNFs-850 (0.81 V), commercial Pt/C (0.84 V), as well as many previously reported Co-based SACs (Table S2). These findings indicate that the atomically dispersed Co-N-C sites, instead of C-N sites, are the main ORR active centers and the importance of graphitization degree for ORR. The Tafel slopes are further calculated to examine the ORR kinetics of the as-synthesized Co-SA@N-CNFs. As displayed in Fig. 4b, the Co-SA@N-CNFs exhibit a Tafel slope of 50 mV dec^{-1}, which is much lower than that of Pt/C (62 mV dec^{-1}), demonstrating the extraordinary ORR kinetics of Co-SA@N-CNFs. As shown in Fig. 4c, the rotating ring-disk electrode (RRDE) measurement suggest that the predominant product generated during the ORR process on Co-SA@N-CNFs is OH^-, instead of undesired peroxide species (H_2O_2). The low yield of H_2O_2 indicates the outstanding catalytic selectivity and efficiency of Co-SA@N-CNFs. The electron-transfer number (n) occurred on Co-SA@N-CNFs approaches to 4, again, indicating a favorable 4-electron ORR
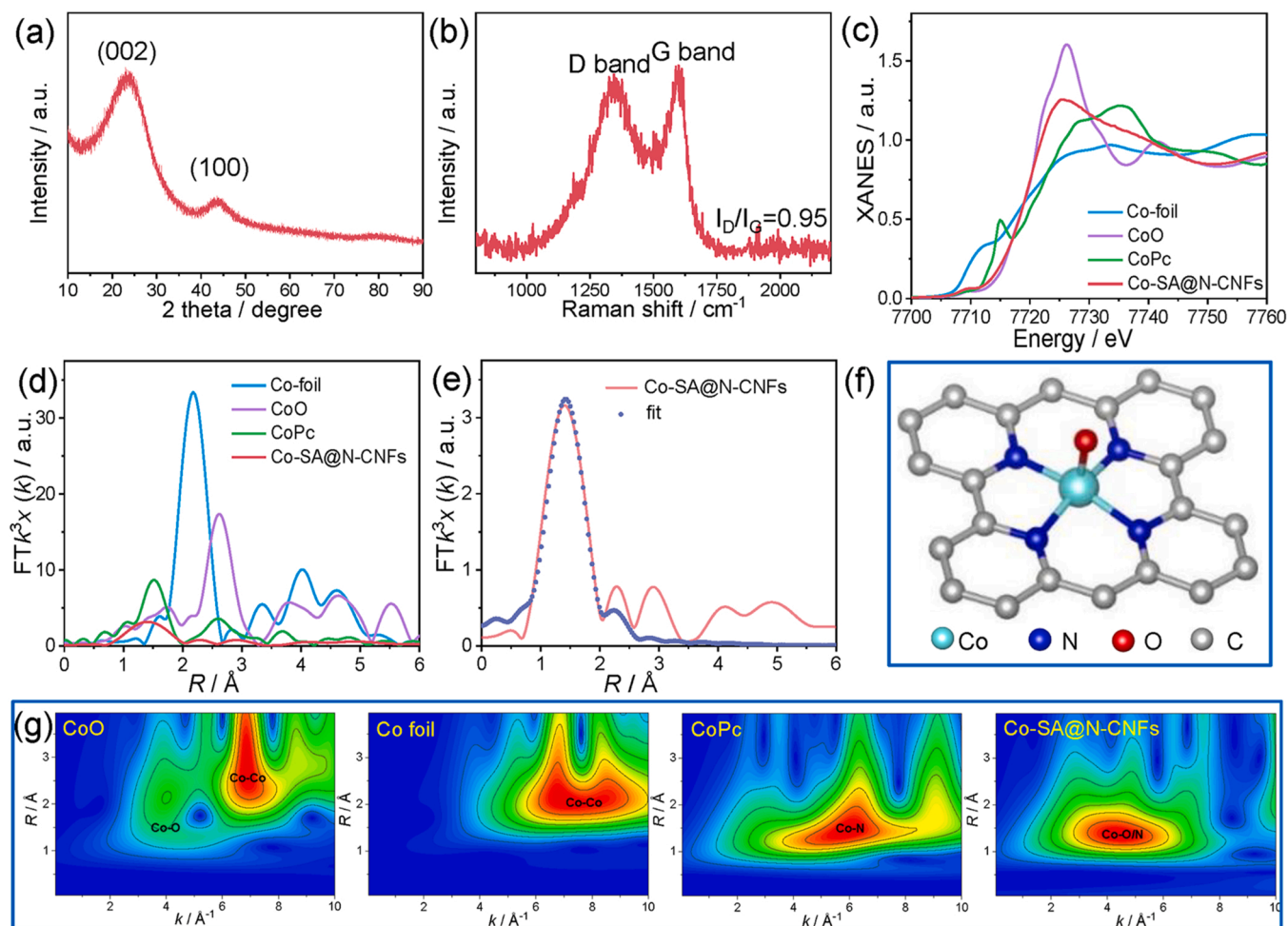
Fig. 3. Compositional examinations and coordination chemistry analyses of the synthesized Co-SA@N-CNFs. (a) XRD pattern, (b) Raman spectrum, (c) XANES curves, (d) FT-EXAFS curves, (e) EXAFS fitting curves, (f) the proposed atomic structure configuration of Co-N$_4$O moiety, (g) WT-EXAFS contour plots of Co-SA@N-CNFs and references.

pathway. To investigate the methanol crossover effect and the stability of Co-SA@N-CNFs, chronoamperometric tests were further performed. As displayed in Fig. 4d, Co-SA@N-CNFs exhibits an exceptional immunity to methanol when 1.0 M methanol is injected into the electrolyte, without any attenuation of current density. By contrast, a sharp decrease of current density happened on Pt/C catalyst under the identical test condition. In addition, during the long-term stability test, Co-SA@N-CNFs shows good stability with 93% retention of current density after a 30000 s test (Fig. S9a), which surpasses the commercial Pt/C (87%) and reflects the excellent electrochemical durability of Co-SA@N-CNFs. TEM image (Fig. S9b) suggests that the 1D fibrous structure of Co-SA@N-CNFs can be well maintained after the stability test. Furthermore, the AC HAADF-STEM image (Fig. S9c) suggests that a large number of isolated bright dots spread homogeneously throughout the entire carbon support, confirming the atomic-level dispersion of the Co single sites after the ORR stability test. The elemental mappings (Fig. S9d) reveal that Co, C, N, and O elements are also homogeneously distributed throughout the carbon nanofibers after stability test. All these findings collectively demonstrate the superb structural robustness of Co-SA@N-CNFs.

3.3. Theoretical simulation of Co-SA@N-CNFs

To reveal the possible origins for the enhanced ORR activity of the Co-SA@N-CNFs, density functional theory (DFT) calculations were further carried out. Normally, for atomically dispersed single Co sites,

the cobalt atom usually coordinates with four N atoms to form a square-planar Co−N$_4$ porphyrin-like structure. While in the present study, the EXAFS fitting results show that the cobalt atom in Co-SA@N-CNFs adopts the coordination model of Co-N$_4$O with one axial O atom perpendicular to the Co−N$_4$ plane. Therefore, two structural models, namely, Co-N$_4$ and Co-N$_4$O, were built to uncover the electrocatalytic ORR mechanisms. As displayed in Fig. 4e, the ORR free energy diagrams of Co−N$_4$ and Co−N$_4$O display the thermodynamically downhill free energy pathways at an ideal electrode potential of $U = 0$ V, revealing that all elementary steps of the electron transfer proceeding on Co−N$_4$ and Co−N$_4$O are exothermic and spontaneous processes. At the standard potential of $U = 1.23$ V, as reflected by the largest uphill Gibbs free energy, the formation of *OOH (the first protonation step) is considered as the rate-determining step (RDS) for Co−N$_4$ and Co−N$_4$O. Notably, Co−N$_4$O possesses a significantly smaller *OOH adsorption free energy of 0.55 eV than that of Co−N$_4$ (0.77 eV), highlighting the promotional effect of the regulation of coordination microenvironment by the introduction of axial O atom. The charge density difference analysis (Fig. 4 f) further confirms that an oriented electron depletion of Co center atoms toward the adjacent axial O can be observed in Co-N$_4$O as compared with Co-N$_4$O, suggesting that the introduction of O atom may induce the electronic reconfiguration and may facilitate the chemisorption and activation of reaction intermediates (e.g., *OOH). More specifically, the *OOH intermediate adsorbed on Co−N$_4$O possesses a charge of 0.461 e^-, which is larger than that on Co−N$_4$ (0.385 e^-). Simultaneously, for the *OOH adsorbed Co−N$_4$O site, the bond length of
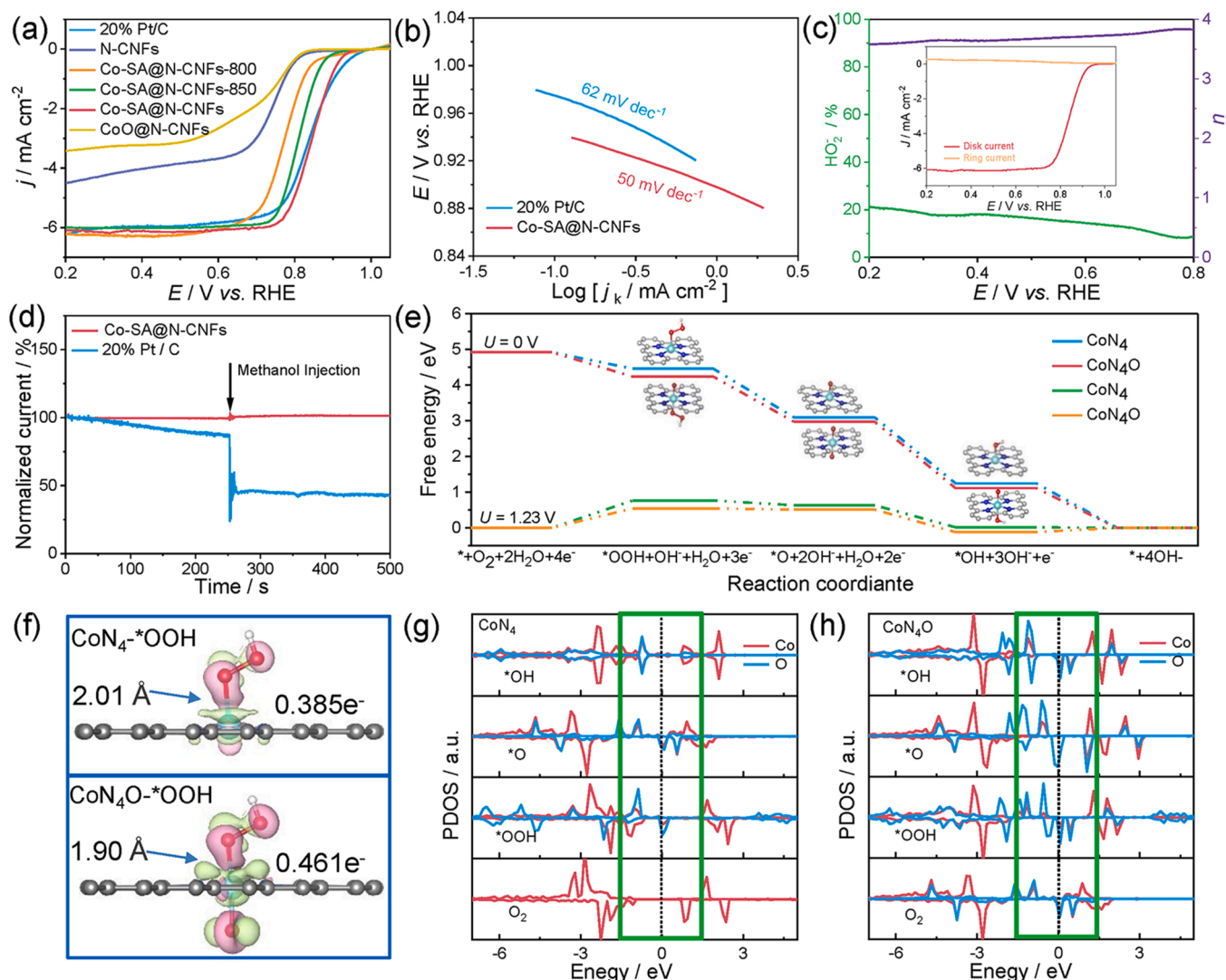
Fig. 4. Electrocatalytic ORR performance evaluation of Co-SA@N-CNFs in 0.1 M KOH medium. (a) ORR polarization curves and reference samples, (b) Tafel plots of Co-SA@N-CNFs and Pt/C, (c) H_2O_2 yield (bottom) and ORR electron transfer number (top) (inset: RRDE curves), (d) methanol tolerance tests of Co-SA@N-CNFs and Pt/C, (e) the calculated free energy diagrams of ORR on CoN_4 and CoN_4O, (f) the calculated charge density differences of the CoN_4 and CoN_4O and the optimized geometries of the *OOH adsorption configurations, (g)-(h) the calculated DOSs of key intermediates on CoN_4 and CoN_4O, respectively.

Co-O is calculated to be 1.90 Å, which is shorter than that on the Co−N$_4$ site (2.01 Å), further affirming that the coordination of Co center with the axial O atom greatly optimizes the binding strengths toward the reaction intermediates and thus dramatically reduce the RDS energy barrier. Fig. 4 g and 4 h display the projected density of states (PDOSs) of Co−N$_4$ and Co−N$_4$O toward various reaction intermediates.[45] Compared with Co−N$_4$, the Co D-orbital of Co−N$_4$O exhibits a higher density state near the Fermi level, indicating enhanced charge carrier density and boosted charge transfer capability conferred by the axially coordinated O atom. In addition, the coordination of axial O atom induces the significant enhancement of charge delocalization, which is advantageous to the adsorption of reaction intermediates and agrees well with the above charge density difference findings. Furthermore, with the regulation of the axial O atom, the Co 3d orbitals in Co−N$_4$O exhibit an increased overlap with the O 2p orbitals, greatly accelerating the electron transfer during the ORR process. All the aforementioned calculation results corroborate the pivotal role of the axial O atom in modulating the local coordination microenvironment of center Co atoms and ultimately boosting the ORR intrinsic activity of Co-SA@N-CNFs.

3.4. Liquid Zn-air battery test

Encouraged by the outstanding ORR activity and superior durability, the as-synthesized Co-SA@N-CNFs are expected to demonstrate promising potential applications in ORR-related electrochemical devices. As a proof-of-concept demonstration, Co-SA@N-CNFs catalyst was firstly applied in a liquid rechargeable Zn–air battery (ZAB). The assembled ZAB consists of a zinc plate as the anode, 6 M KOH and 0.2 M ZnCl$_2$ solution as the alkaline aqueous electrolyte, and catalyst-loaded conductive carbon paper as the air cathode, as diagrammatically sketched in Fig. 5a. The air cathode catalyst is composed of Co-SA@N-CNFs and commercial RuO$_2$ (for the oxygen evolution reaction) with a mass ratio of 1: 1. Additionally, a ZAB equipped using a mixture of commercial Pt/C and RuO$_2$ (1: 1 in mass ratio) is also appraised under the same test conditions for comparison. As displayed in Fig. 5b, the Co-SA@N-CNFs+RuO$_2$-assembled ZAB delivers a stable open-circuit voltage (OCV) of 1.47 V, which is higher than that of the Pt/C+RuO$_2$-based counterpart (1.44 V). As an exemplification, three Co-SA@N-CNFs+RuO$_2$-assembled ZABs connected in a series can illuminate a light-emitting diode (LED, ~3 V) screen for several hours (Fig. 5c), affirming the promising practicability of Co-SA@N-CNFs. The discharge
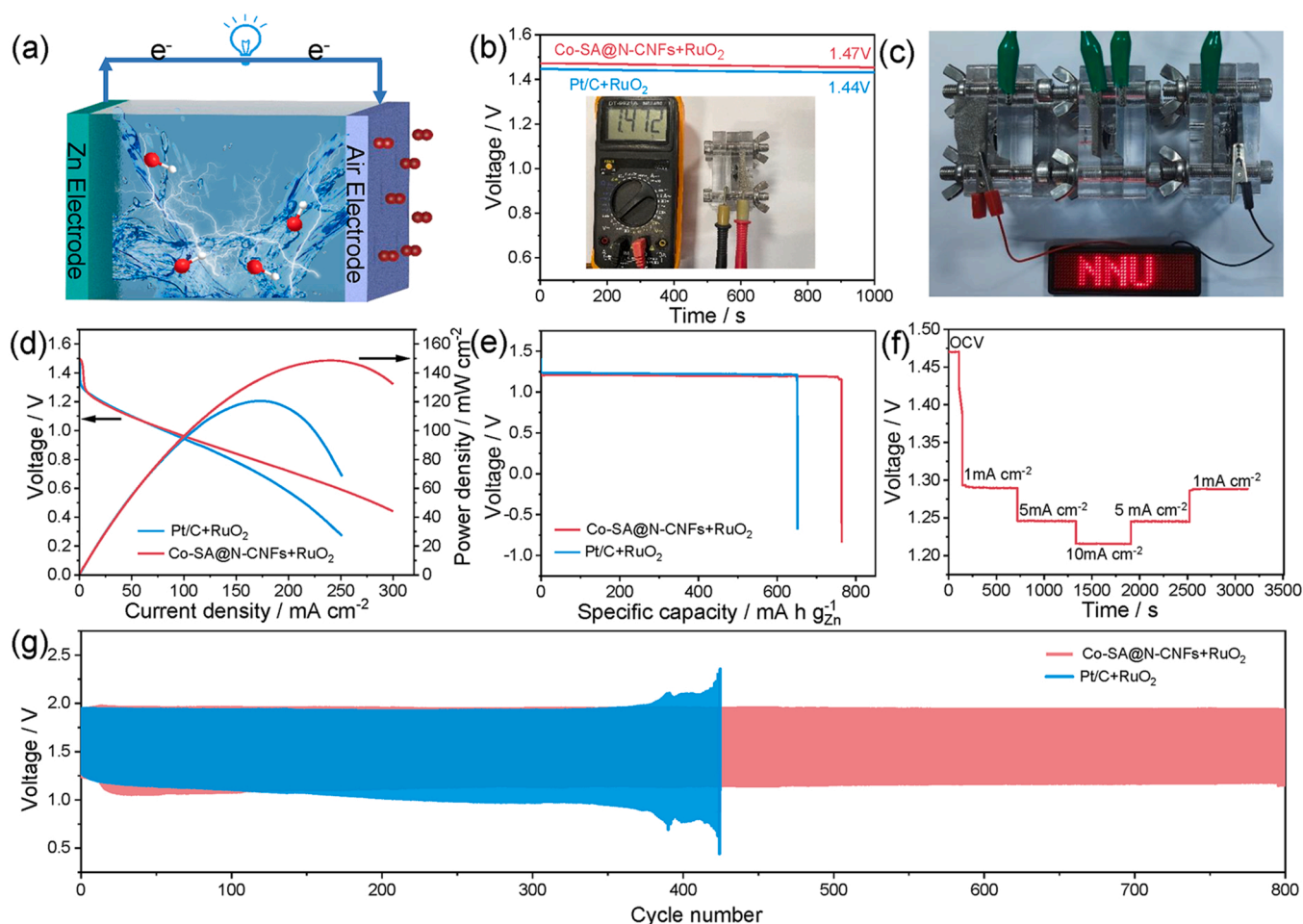
Fig. 5. Liquid ZAB performance comparisons of Co-SA@N-CNFs+RuO$_2$ couple and Pt/C+RuO$_2$ couple. (a) Schematic illustration of the liquid ZAB configuration, (b) OCV curves, (c) photograph of LED screen powered by three tandem ZABs, (d) discharge polarization plots and power density curves, (e) specific capacities, (f) rate performance tests, and (g) galvanostatic change-discharge voltage profiles.

polarization plots (Fig. 5d) reveal that the Co-SA@N-CNFs-based ZAB delivers a maximum power density of 173.1 mW cm^{-2}, which is larger than that of the Pt/C benchmark (138.8 mW cm^{-2}) and a majority of previously reported non-precious catalyst-built ZABs (Table S3). In addition, based on the consumed Zn mass, the Co-SA@N-CNFs-driven ZAB delivers a specific discharge capacity of 764 mA h g$_{Zn}^{-1}$ at 10 mA cm^{-2}, which is corresponding to the energy density of 916.8 W h kg$_{Zn}^{-1}$. Whereas, the Pt/C-based ZAB exhibits a lower specific capacity of 651 mA h g$_{Zn}^{-1}$ and an energy density of 797.5 W h kg$_{Zn}^{-1}$ (Fig. 5e). The rate performance of the Co-SA@N-CNFs+RuO$_2$-constructed ZAB is evaluated by the galvanostatic discharging tests at different current densities (1, 5 and 10 mA cm^{-2}, respectively). As shown in Fig. 5f, as the current density increases step by step, the discharging voltage plateau decreases correspondingly. Moreover, the discharging voltages can be well recovered to the original level without apparent voltage drop when the current densities are back to the initial value, demonstrating excellent rate performance and superior reversibility of the Co-SA@N-CNFs+RuO$_2$-constructed ZAB. The long-life cycling stabilities of the two equipped ZABs are examined at a current density of 5 mA cm^{-2} with a 20-min galvanostatic charging/discharging duration per cycle. Fig. 5g demonstrates that the Co-SA@N-CNFs+RuO$_2$-constructed ZAB exhibits a negligible performance fading even after the continuous operation of 800 cycles (about 266.7 h). While for the Pt/C+RuO$_2$-based ZAB, the charging-discharging voltage gap increases drastically after only 420 cycles (about 140 h) and causes serious activity degradation.

3.5. Flexible Zn-air battery test

Motivated by the ever-increasing demands of flexible and wearable electronic devices, we have further assembled a flexible rechargeable all-solid-state ZAB, which employs zinc plate as the anode and Co-SA@N-CNFs+RuO$_2$ coated carbon cloth as the cathode sandwiched with polyacrylic acid (PAA)/KOH gel as the solid electrolyte (Fig. 6a). The assembled solid-state ZAB delivers a high OCV of 1.48 V (Fig. 6b). Three tandem Co-SA@N-CNFs-based solid-state ZABs are successfully capable of lighting a LED screen (Fig. 6c), implying the practical potentials in wearable electronic devices. Fig. 6d shows the discharge polarization plot and the corresponding power density curve. It can be found that the Co-SA@N-CNFs-based solid-state ZAB exhibits a peak power density of 76.3 mW cm^{-2}, exceeding most of the recently reported advanced electrocatalysts (Table S4). Fig. 6e displays the discharge curves of the flexible Co-SA@N-CNFs-assembled ZAB at various current densities. The discharging plateaus exhibit excellent recovery capability without significant voltage decay when the current density is restored, indicating the superior rate capability of Co-SA@N-CNFs. Furthermore, the cycling rechargeability of the Co-SA@N-CNFs-assembled solid-state ZAB is further investigated at a current density of 1 mA cm^{-2} with a duration of 20 min per cycle. As shown in Fig. 6f, the slight voltage fading and the steady performance of the solid-state ZAB over 36 cycles (12 h) verify the excellent reversibility and stability of the Co-SA@N-CNFs-assembled solid-state ZAB. More impressively, even after the test for 6 h with severe structural changes (from unbent to different bending angles), the discharging and charging voltage profiles of the assembled solid-state
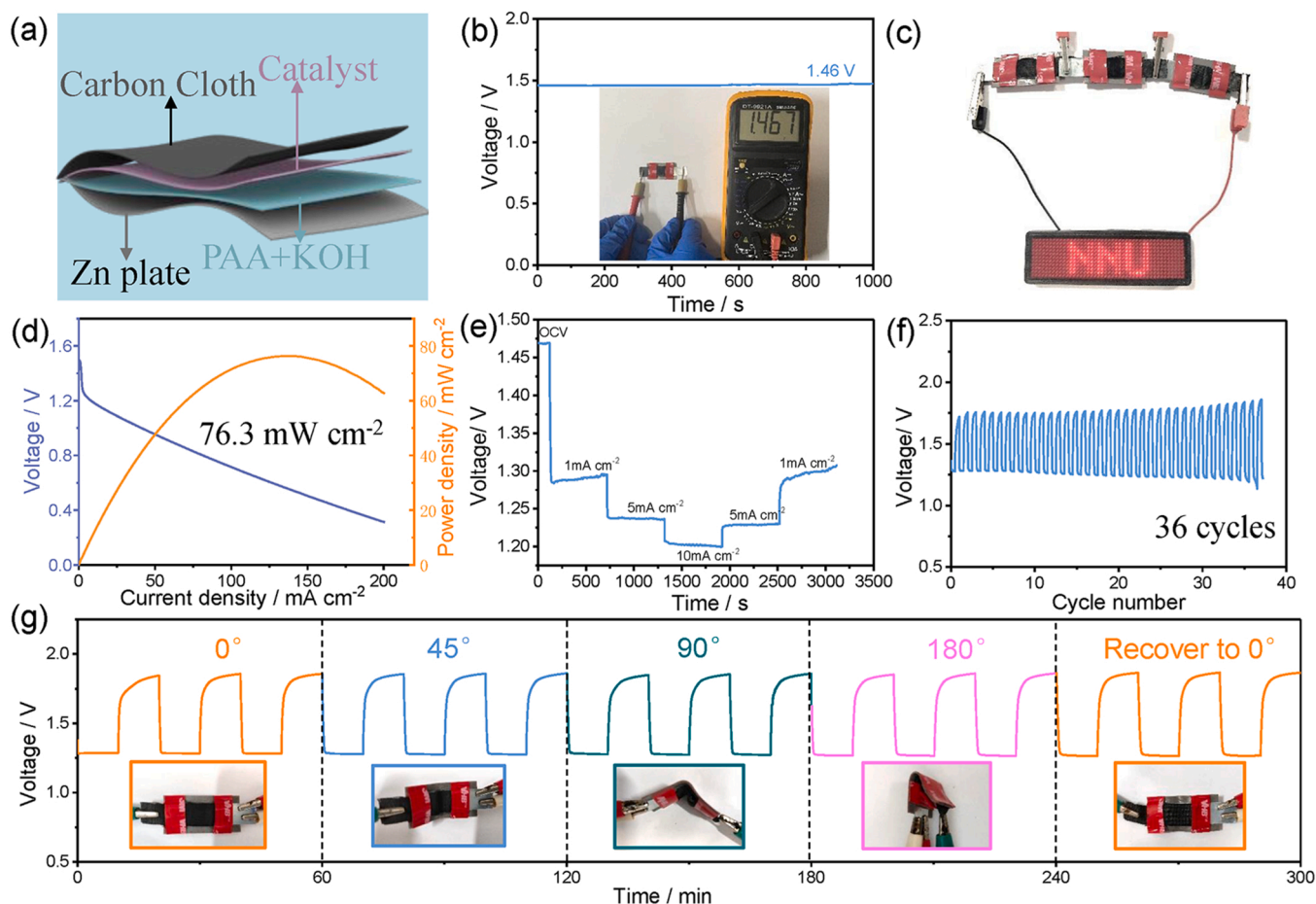
Fig. 6. Electrochemical performance of the solid state ZAB assembled by Co-SA@N-CNFs+RuO$_2$ couple. (a) Schematic illustration of the flexible solid-state ZAB configuration, (b) OCV curve, (c) photograph of LED screen lit by three tandem solid state ZABs, (d) discharge polarization plot and the corresponding power density curve, (e) discharging plateaus at different current densities, (f) cycling performance profiles for 36 cycles, (g) cycling profiles upon different mechanical deformations.

ZAB almost keep identical and thus maintain extremely stable, demonstrating the superb mechanical flexibility and promising application potential in wearable and flexible electronic devices.

4. Conclusion

To sum up, we have developed a facile and robust "phenolic resin-bridged" approach for the gram-scale fabrication of atomically dispersed Co sites confined on N-doped carbon nanofibers for efficient oxygen reduction electrocatalysis. Comprehensive experimental characterizations collectively demonstrate that the coordination configuration of the single-atomic Co sites is the Co-N$_4$O moiety with one O atom in the axial direction perpendicular to the Co-N$_4$ plane. Profiting from the high density of single atomic Co active sites and fibrous conductive networked highways for mass transport and electron transfer, the as-fabricated Co-SA@N-CNFs exhibit superior ORR activity, outstanding long-term stability and high methanol tolerance in alkaline media, surpassing the benchmark Pt/C catalyst and most of the recently reported non-precious ORR electrocatalysts. DFT calculations reveal that, compared with the conventional Co-N$_4$ single sites, the construction of Co-N$_4$O moiety with the axial O coordination atom could effectively reduce the reaction energy barriers, tune the bond length between the metal sites and the intermediates, and enhance the electron transfer capability, consequently reducing the reaction energy barrier and exhibiting extraordinary intrinsic ORR activity. Moreover, the Co-SA@N-CNFs assembled liquid and flexible solid-state rechargeable ZABs also deliver higher power densities and specific capacities, as well

as superior cycling stability, compared with the Pt/C-based counterpart. The present study not only develops a straightforward and reliable strategy for the scalable synthesis of SACs, but also provides a deep insight into the modulation of the metal coordination configuration of the single-atom sites toward the enhancement of electrocatalytic performance.

CRediT authorship contribution statement

Sike Zhang: Investigation, Visualization, Writing – original draft, Writing – review & editing, Formal analysis. **Qixing Zhou:** Investigation, Visualization, Writing – original draft, Writing – review & editing, Formal analysis. **Linya Fang:** Investigation, Visualization, Formal analysis, the supporting of contribution. **Rui Wang:** Formal analysis, the supporting of contribution. **Tingyu Lu:** Formal analysis, the supporting of contribution. **Qun Zhao:** Investigation, Visualization, Writing – review & editing, Formal analysis. **Xuefang Gu:** Investigation, Visualization, Writing – review & editing, Formal analysis. **Shu Tian:** Investigation, Visualization, Writing – review & editing, Formal analysis. **Lin Xu:** Conceptualization, Formal analysis, Funding acquisition, Supervision, Visualization, Writing – review & editing. **Huan Pang:** Investigation, Visualization, Writing – review & editing, Formal analysis. **Jun Yang:** Investigation, Visualization, Writing – review & editing, Formal analysis. **Yawen Tang:** Conceptualization, Formal analysis, Funding acquisition, Supervision, Visualization, Writing – review & editing. **Shuhui Sun:** Conceptualization, Formal analysis, Supervision, Visualization, Writing – review & editing.

Declaration of Competing Interest

The authors declare that they have no known competing financial interests or personal relationships that could have appeared to influence the work reported in this paper.

Data availability

Data will be made available on request.

Appendix A. Supporting information

Supplementary data associated with this article can be found in the online version at doi:10.1016/j.apcatb.2023.122489.

References

[1] A. Zitolo, N. Ranjbar-Sahraie, T. Mineva, J. Li, Q. Jia, S. Stamatin, G.F. Harrington, S.M. Lyth, P. Krtil, S. Mukerjee, E. Fonda, F. Jaouen, Identification of catalytic sites in cobalt-nitrogen-carbon materials for the oxygen reduction reaction, Nat. Commun. 8 (2017) 957, https://doi.org/10.1038/s41467-017-01100-7.

[2] M. Wu, G. Zhang, M. Wu, J. Prakash, S. Sun, Rational design of multifunctional air electrodes for rechargeable Zn–Air batteries: recent progress and future perspectives, Energy Storage Mater. 21 (2019) 253–286, https://doi.org/10.1016/j.ensm.2019.05.018.

[3] D. Yang, D. Chen, Y. Jiang, E.H. Ang, Y. Feng, X. Rui, Y. Yu, Carbon-based materials for all-solid-state zinc–air batteries, Carbon Energy 3 (2021) 50–65, https://doi.org/10.1002/cey2.88.

[4] Q. Jin, B. Ren, H. Cui, C. Wang, Nitrogen and cobalt co-doped carbon nanotube films as binder-free trifunctional electrode for flexible zinc-air battery and self-powered overall water splitting, Appl. Catal. B: Environ. 283 (2021), 119643, https://doi.org/10.1016/j.apcatb.2020.119643.

[5] I.E.L. Stephens, J. Rossmeisl, I. Chorkendorff, Toward sustainable fuel cells, Science 354 (2016) 1378–1379, https://doi.org/10.1126/science.aal3303.

[6] X.X. Wang, D.A. Cullen, Y.T. Pan, S. Hwang, M. Wang, Z. Feng, J. Wang, M. H. Engelhard, H. Zhang, Y. He, Y. Shao, D. Su, K.L. More, J.S. Spendelow, G. Wu, Nitrogen-coordinated single cobalt atom catalysts for oxygen reduction in proton exchange membrane fuel cells, Adv. Mater. 30 (2018) 1706758, https://doi.org/10.1002/adma.201706758.

[7] I. Jiménez-Morales, A. Reyes-Carmona, M. Dupont, S. Cavaliere, M. Rodlert, F. Mornaghini, M.J. Larsen, M. Odgaard, J. Zajac, D.J. Jones, J. Rozière, Correlation between the surface characteristics of carbon supports and their electrochemical stability and performance in fuel cell cathodes, Carbon Energy 3 (2021) 654–665, https://doi.org/10.1002/cey2.109.

[8] Z. Li, X. Jiang, X. Wang, J. Hu, Y. Liu, G. Fu, Y. Tang, Concave PtCo nanocrosses for methanol oxidation reaction, Appl. Catal. B: Environ. 277 (2020), 119135, https://doi.org/10.1016/j.apcatb.2020.119135.

[9] A.J. Martín, J. Pérez-Ramírez, Heading to distributed electrocatalytic conversion of small abundant molecules into fuels, chemicals, and fertilizers, Joule 3 (2019) 2602–2621, https://doi.org/10.1016/j.joule.2019.09.007.

[10] Y. Tian, X. Liu, L. Xu, D. Yuan, Y. Dou, J. Qiu, H. Li, J. Ma, Y. Wang, D. Su, S. Zhang, Engineering crystallinity and oxygen vacancies of Co(II) oxide nanosheets for high performance and robust rechargeable Zn-air batteries, Adv. Funct. Mater. 31 (2021) 2101239, https://doi.org/10.1002/adfm.202101239.

[11] M. Xiao, Y. Chen, J. Zhu, H. Zhang, X. Zhao, L. Gao, X. Wang, J. Zhao, J. Ge, Z. Jiang, S. Chen, C. Liu, W. Xing, Climbing the apex of the ORR volcano plot via binuclear site construction: electronic and geometric engineering, J. Am. Chem. Soc. 141 (2019) 17763–17770, https://doi.org/10.1021/jacs.9b08362.

[12] X. Tong, X. Zhan, D. Rawach, Z. Chen, G. Zhang, S. Sun, Low-dimensional catalysts for oxygen reduction reaction, Prog. Nat. Sci. Mater. Inter 30 (2020) 787–795, https://doi.org/10.1016/j.pnsc.2020.09.011.

[13] F. Dong, M. Wu, Z. Chen, X. Liu, G. Zhang, J. Qiao, S. Sun, Atomically dispersed transition metal-nitrogen-carbon bifunctional oxygen electrocatalysts for zinc-air batteries: recent advances and future perspectives, Nano-Micro Lett. 14 (2021) 36, https://doi.org/10.1007/s40820-021-00768-3.

[14] Y. Wang, H. Su, Y. He, L. Li, S. Zhu, H. Shen, P. Xie, X. Fu, G. Zhou, C. Feng, Advanced electrocatalysts with single-metal-atom active sites, Chem. Rev. 120 (2020) 12217–12314, https://doi.org/10.1021/acs.chemrev.0c00594.

[15] H. Shang, X. Zhou, J. Dong, A. Li, X. Zhao, Q. Liu, Y. Lin, J. Pei, Z. Li, Z. Jiang, Engineering unsymmetrically coordinated Cu-S₁N₃ single atom sites with enhanced oxygen reduction activity, Nat. Commun. 11 (2020) 1–11, https://doi.org/10.1038/s41467-020-16848-8.

[16] Y. Cao, S. Chen, Q. Luo, H. Yan, Y. Lin, W. Liu, L. Cao, J. Lu, J. Yang, T. Yao, S. Wei, Atomic-level insight into optimizing the hydrogen evolution pathway over a Co₁-N₄ single-site photocatalyst, Angew. Chem. Int. 56 (2017) 12191–12196, https://doi.org/10.1002/anie.201706467.

[17] D. Gao, T. Liu, G. Wang, X. Bao, Structure sensitivity in single-atom catalysis toward CO₂ electroreduction, ACS Energy Lett. 6 (2021) 713–727, https://doi.org/10.1021/acsenergylett.0c02665.

[18] L. Shen, M. Ma, F. Tu, Z. Zhao, Y. Xia, K. Goh, L. Zhao, Z. Wang, G. Shao, Recent advances in high-loading catalysts for low-temperature fuel cells: from nanoparticle to single atom, SusMat 1 (2021) 569–592, https://doi.org/10.1002/sus2.38.

[19] Y. Mu, T. Wang, J. Zhang, C. Meng, Y. Zhang, Z. Kou, Single-atom catalysts: advances and challenges in metal-support interactions for enhanced electrocatalysis, Electrochem. Energy Rev. 5 (2022) 145–186, https://doi.org/10.1007/s41918-021-00124-4.

[20] Z. Chen, X. Liao, C. Sun, K. Zhao, D. Ye, J. Li, G. Wu, J. Fang, H. Zhao, J. Zhang, Enhanced performance of atomically dispersed dual-site Fe-Mn electrocatalysts through cascade reaction mechanism, Appl. Catal. B: Environ. 288 (2021), 120021, https://doi.org/10.1016/j.apcatb.2021.120021.

[21] M. Mazzucato, G. Daniel, A. Mehmood, T. Kosmala, G. Granozzi, A. Kucernak, C. Durante, Effects of the induced micro- and meso-porosity on the single site density and turn over frequency of Fe-N-C carbon electrodes for the oxygen reduction reaction, Appl. Catal. B: Environ. 291 (2021), 120068, https://doi.org/10.1016/j.apcatb.2021.120068.

[22] Y. Meng, J.-C. Li, S.-Y. Zhao, C. Shi, X.-Q. Li, L. Zhang, P.-X. Hou, C. Liu, H.-M. Cheng, Fluorination-assisted preparation of self-supporting single-atom Fe-N-doped single-wall carbon nanotube film as bifunctional oxygen electrode for rechargeable Zn-Air batteries, Appl. Catal. B: Environ. 294 (2021), 120239, https://doi.org/10.1016/j.apcatb.2021.120239.

[23] J. Li, P. Pršlja, T. Shinagawa, A.J. Martín Fernández, F. Krumeich, K. Artyushkova, P. Atanassov, A. Zitolo, Y. Zhou, R. García-Muelas, N. López, J. Pérez-Ramírez, F. Jaouen, Volcano trend in electrocatalytic CO₂ reduction activity over atomically dispersed metal sites on nitrogen-doped carbon, ACS Catal. 9 (2019) 10426–10439, https://doi.org/10.1021/acscatal.9b02594.

[24] J. Wang, Z. Huang, W. Liu, C. Chang, H. Tang, Z. Li, W. Chen, C. Jia, T. Yao, S. Wei, Y. Wu, Y. Li, Design of N-coordinated dual-metal sites: a stable and active Pt-free catalyst for acidic oxygen reduction reaction, J. Am. Chem. Soc. 139 (2017) 17281–17284, https://doi.org/10.1021/jacs.7b10385.

[25] Z. Xu, W. Deng, X. Wang, 3D hierarchical carbon-rich micro-/nanomaterials for energy storage and catalysis, Electrochem. Energy Rev. 4 (2021) 269–335, https://doi.org/10.1007/s41918-021-00094-7.

[26] X. Ge, G. Su, W. Che, J. Yang, X. Zhou, Z. Wang, Y. Qu, T. Yao, W. Liu, Y. Wu, Atomic filtration by graphene oxide membranes to access atomically dispersed single atom catalysts, ACS Catal. 10 (2020) 10468–10475, https://doi.org/10.1021/acscatal.0c02203.

[27] S. Ji, Y. Chen, X. Wang, Z. Zhang, D. Wang, Y. Li, Chemical synthesis of single atomic site catalysts, Chem. Rev. 120 (2020) 11900–11955, https://doi.org/acs.chemrev.9b00818.

[28] H. Fei, J. Dong, Y. Feng, C.S. Allen, C. Wan, B. Volosskiy, M. Li, Z. Zhao, Y. Wang, H. Sun, P. An, W. Chen, Z. Guo, C. Lee, D. Chen, I. Shakir, M. Liu, T. Hu, Y. Li, A. I. Kirkland, X. Duan, Y. Huang, General synthesis and definitive structural identification of MN₄C₄ single-atom catalysts with tunable electrocatalytic activities, Nat. Catal. 1 (2018) 63–72, https://doi.org/s41929-017-0008-y.

[29] Z. Zhang, X. Zhao, S. Xi, L. Zhang, Z. Chen, Z. Zeng, M. Huang, H. Yang, B. Liu, S. J. Pennycook, P. Chen, Atomically dispersed cobalt trifunctional electrocatalysts with tailored coordination environment for flexible rechargeable Zn-Air battery and self-driven water splitting, Adv. Energy Mater. 10 (2020) 2002896, https://doi.org/10.1002/aenm.202002896.

[30] Y. Ha, B. Fei, X. Yan, H. Xu, Z. Chen, L. Shi, M. Fu, W. Xu, R. Wu, Atomically dispersed Co-pyridinic N-C for superior oxygen reduction reaction, Adv. Energy Mater. 10 (2020) 2002592, https://doi.org/10.1002/aenm.202002592.

[31] L. Chen, X. Liu, L. Zheng, Y. Li, X. Guo, X. Wan, Q. Liu, J. Shang, J. Shui, Insights into the role of active site density in the fuel cell performance of Co-N-C catalysts, Appl. Catal. B: Environ. 256 (2019), 117849, https://doi.org/10.1016/j.apcatb.2019.117849.

[32] L. Zhang, N. Shang, S. Gao, J. Wang, T. Meng, C. Du, T. Shen, J. Huang, Q. Wu, H. Wang, Y. Qiao, C. Wang, Y. Gao, Z. Wang, Atomically dispersed Co catalyst for efficient hydrodeoxygenation of lignin-derived species and hydrogenation of nitroaromatics, ACS Catal. 10 (2020) 8672–8682, https://doi.org/10.1021/acscatal.0c00239.

[33] X. Zhang, P. Zhai, Y. Zhang, Y. Wu, C. Wang, L. Ran, J. Gao, Z. Li, B. Zhang, Z. Fan, L. Sun, J. Hou, Engineering Single-Atomic Ni-N₄-O Sites on Semiconductor Photoanodes for High-Performance Photoelectrochemical Water Splitting, J. Am. Chem. Soc. (2021) 20657–20669, https://doi.org/10.1021/jacs.1c07391.

[34] M.B. Gawande, P. Fornasiero, R. Zbořil, Carbon-based single-atom catalysts for advanced applications, ACS Catal. 10 (2020) 2231–2259, https://doi.org/10.1021/acscatal.9b04217.

[35] S. Wang, H. Wang, C. Huang, P. Ye, X. Luo, J. Ning, Y. Zhong, Y. Hu, Trifunctional electrocatalyst of N-doped graphitic carbon nanosheets encapsulated with CoFe alloy nanocrystals: the key roles of bimetal components and high-content graphitic-N, Appl. Catal. B: Environ. 298 (2021) 120512, https://doi.org/10.1016/j.apcatb.2021.120512.

[36] Y. Han, Y. Wang, R. Xu, W. Chen, L. Zheng, A. Han, Y. Zhu, J. Zhang, H. Zhang, J. Luo, C. Chen, Q. Peng, D. Wang, Y. Li, Electronic structure engineering to boost oxygen reduction activity by controlling the coordination of the central metal, Energy Environ. Sci. 11 (2018) 2348–2352, https://doi.org/10.1039/c8ee01481g.

[37] M. Li, M. Wang, D. Liu, Y. Pan, S. Liu, K. Sun, Y. Chen, H. Zhu, W. Guo, Y. Li, Z. Cui, B. Liu, Y. Liu, C. Liu, Atomically-dispersed NiN4-Cl active sites with axial Ni-Cl coordination for accelerating electrocatalytic hydrogen evolution, J. Mater. Chem. A 10 (2022) 6007–6015, https://doi.org/10.1039/D1TA08287F.

[38] C. Ye, N. Zhang, D. Wang, Y. Li, Single atomic site catalysts: synthesis, characterization, and applications, Chem. Commun. 56 (2020) 7687–7697, https://doi.org/10.1039/d0cc03221b.

[39] Z. Song, L. Zhang, K. Doyle-Davis, X. Fu, J.L. Luo, X. Sun, Recent Advances in MOF-Derived Single Atom Catalysts for Electrochemical Applications, Adv. Energy Mater. 10 (2020) 2001561, https://doi.org/10.1002/aenm.202001561.

[40] L. Peng, L. Shang, T. Zhang, G.I.N. Waterhouse, Recent advances in the development of single-atom catalysts for oxygen electrocatalysis and zinc-air batteries, Adv. Energy Mater. 10 (2020) 2003018, https://doi.org/10.1002/aenm.202003018.

[41] Y. Chen, Z. Li, Y. Zhu, D. Sun, X. Liu, L. Xu, Y. Tang, Atomic Fe dispersed on N-doped carbon hollow nanospheres for high-efficiency electrocatalytic oxygen reduction, Adv. Mater. 31 (2019) 1806312, https://doi.org/10.1002/adma.201806312.

[42] Y. Tian, L. Xu, M. Li, D. Yuan, X. Liu, J. Qian, Y. Dou, J. Qiu, S. Zhang, Interface engineering of CoS/CoO@N-doped graphene nanocomposite for high-performance rechargeable Zn-Air, Batter., Nano-Micro Lett. 13 (2020) 3, https://doi.org/10.1007/s40820-020-00526-x.

[43] Q. Yu, J. Lv, Z. Liu, M. Xu, W. Yang, K.A. Owusu, L. Mai, D. Zhao, L. Zhou, Macroscopic synthesis of ultrafine N-doped carbon nanofibers for superior capacitive energy storage, Sci. Bull. 64 (2019) 1617–1624, https://doi.org/10.1016/j.scib.2019.08.008.

[44] Q. Zhou, S. Hou, Y. Cheng, R. Sun, W. Shen, R. Tian, J. Yang, H. Pang, L. Xu, K. Huang, Y. Tang, Interfacial engineering Co and MnO within N,S co-doped carbon hierarchical branched superstructures toward high-efficiency electrocatalytic oxygen reduction for robust Zn-air batteries, Appl. Catal. B: Environ. 295 (2021), 120281, https://doi.org/10.1016/j.apcatb.2021.120281.

[45] T. Dai, X. Zhang, M. Sun, B. Huang, N. Zhang, P. Da, R. Yang, Z. He, W. Wang, P. Xi, C.H. Yan, Uncovering the promotion of CeO2/CoS1.97 heterostructure with specific spatial architectures on oxygen evolution reaction, Adv. Mater. 33 (2021) 2102593, https://doi.org/10.1002/adma.202102593.